

## Fusion of Synthetic Aperture Radar Images and Optical Images Using Curvelet Transform and Retina Model

Mina Solhi<sup>\*a</sup>, Mehran Yazdi<sup>b</sup>, Mahmoud Sharzehei<sup>c</sup>

<sup>a</sup>Master of Communication Engineering, Shiraz University, Shiraz, Iran.

<sup>b</sup>Associate Professor of Communication Engineering, Shiraz University, Shiraz, Iran.

<sup>c</sup>Assistant Professor of Communication Engineering, Institute of Mechanics, Iranian Space Research Center.

---

Received 4 December 2019; revised 10 January 2020; accepted 10 March 2020

---

### Abstract

In recent years, various image integration techniques have been developed to improve their quality. In this paper, some image integration techniques such as Intensity-Hue-Saturation (HIS), Brovey transform, feedback, non-feedback retina model, wavelet transform, and curvelet transform are investigated to improve the spectral and spatial information of satellite images. Also, a new algorithm has been proposed to improve the image quality resulting from the combination of SAR and visible-like images. In the proposed method, the curvelet transform is first applied to the three input levels of Synthetic Aperture Radar (SAR) and visible-like images, then using horizontal cells in the feedback retina model, spectral and spatial information below a specified and adjustable frequency is determined by a Gaussian low-pass filter and replaced with the curvelet coefficients of the integrated image approximation sub-band. Moreover, fine1 and detail1 sub-bands are selected from the visible-like image, and the coefficients of fine2, detail2 sub-bands are weighted and aggregated from both SAR and visible-like images in a specific way. Spectral and spatial quality evaluation criteria including Quality Index (Q<sub>I</sub>), Measure the Quality of edges (Q<sup>(AB/f)</sup>) Relative Dimensionless Global Error in System (ERGAS), Mutual Information (MI), Euclidian Distance (ED) and Standard Deviation (STD) were used to compare and analyze the results of the methods. The results of this evaluation indicated the remarkable performance of the proposed method in preserving the spectral and spatial information content of the integrated image compared to other methods.

**Keywords:** Fusion, SAR Image, Optic Image, Curvelet Transform, Feedback Retina Model.

---

\* Corresponding author Tel: +98-9175609532.  
Email address: [mina.solhi.95@gmail.com](mailto:mina.solhi.95@gmail.com)

## 1. Introduction

The use of data integration systems has significant advantages such as increased quality, noise, and unreliable data reduction. Therefore, it is necessary to utilize data integration methods in management applications, position monitoring, and troubleshooting. In fact, because of the complexity of various systems, including robotic, mechanical, security, and military, there is no solution except to use the information of multiple sensors and integrate their data.

In recent decades, data and image integration from multiple sensors has been the subject of great attention. The expansion and development of researches on image integration are largely due to recent advances in the optimal use of sensor technology and the enhanced image resolution capacity provided by them. Imaging techniques using multiple sensors have provided a new-emerging field of research on the integration of remote sensing and satellite imagery, security and surveillance systems, etc. Improving the performance of imaging systems requires increasing number of processing units and deploying high-speed DSPs that are very expensive. Therefore, providing appropriate algorithms for image integration at the pixel level is an efficient solution (Khazaei, 2015).

Visible band sensors are capable of capturing very good images of the Earth's surface, though the presence of clouds or darkness interferes with their performance. On the contrary, radar systems are capable of capturing images every day and night, in atmosphere (Lau et al., 2000). The differences between synthetic aperture radar (SAR) and visible systems can be summarized as follows (Shahab pour and Yazdi, 2013).

- SAR systems have a microwave source, while visible band sensors require sunlight or thermal radiation.
- SAR waves are able to pass through the cloud and can be used during the night in different weather conditions. In addition, due to the frequency and polarization of the waves, they may be able to pass through vegetation, sand, and snow.
- SAR radar images can be formed at different polarities and frequencies and more information could be collected about the target.

These differences are very useful for examining and classifying the study areas, because complementary and redundant information from both image sources are integrated into one image, making it easier to identify details and their variations (Mitchell, 2007). Image integration is done at three different levels of pixel, attribute and decision making, where pixel-level models are known as image level or image integration methods (Sun and Deng, 2012). By integrating images in pixel-level, the amount of data that needs to be processed without losing useful information is effectively reduced. In general, the pixel-level integration process is based on multi-resolution transforms, statistical methods, color theory algorithms, or combinatorial techniques. In recent years, integration algorithms based on multi-resolution analysis tools have become increasingly important. Most multi-resolution image processing techniques are based on sophisticated algorithms. Applications of these image processing methods were first introduced by (Burt and Adelson, 1983).

One of the most common multi-color processing methods is wavelet transform, which provides the background for analyzing images into a number of different frequency sub-bands. These sub-bands have different resolution level that can perform complete image recovery. Wavelet transform has the capacity of extracting information and content of images in both frequency and spatial domains, while using the multi-resolution property of wavelet transform and controlling the number of decomposition surfaces, the quality of integration can be determined. Curvelet transform is also one of the most popular multi-color transforms proposed by (Candes et al., 1999). Curvelet transform is the optimal non-adaptive expression of edges and can better fit the image properties. This transform offers edge and other features along the curves much more efficiently than traditional transforms. Curvelet transform analyzing the curved edges is suited to integrate images with high accuracy to approximate and describe the scattering and direction. Discrete and static wavelet transforms are the best tools for image integration. Curvelet transform uses these two tools to integrate images (Li and Yang, 2008). In fact, curvelet transform is a new member of the multi-resolution transform family that has been developed over the past few years to address the weaknesses of traditional multi-resolution transforms such as wavelet transform. In recent years, there has been a great deal of studies on the integration of remote sensing images in the multi-resolution transforms as well as using other methods at the pixel level. It will be discussed in the following:

(Agrawal and Karar, 2018), first applied curvelet transform to visible-like and infrared images, then

integrated the curvelet coefficients of the images approximation sub-band with PCA method and the coefficients of the detail and fine sub-band with the maximum absolute value principle.

(Shokrallahi and Sahebi, 2017), first applied curvelet transform to SAR and visible-like images in five decomposition levels, then selected and integrated the coefficients of approximation, detail1, detail2, fine1, and fine2 from the visible-like image and the coefficients of detail3, detail4, fine3, and fine4 from both the visible-like and SAR images by thresholding the convergence coefficient of curvelet coefficients.

(Dong et al., 2015), first transferred the multispectral image bands from the RGB to the IHS space, then, applying the curvelet transform in the resulting intensity component and the panchromatic image, considering the standard deviation, integrated the resulting curvelet coefficients increasing the accuracy of spatial content.

(Pappas et al., 2013), applied curvelet transform to single-band panchromatic and SAR images and then integrated the resulting coefficients based on weighted average.

(Ghasemian et al., 2011), integrated panchromatic and visible-like images based on the feedback and no-feedback retina model. Inspired by the human retina and using two Gaussian low-pass filters with different frequency bands, they first extracted the low-frequency content from the visible-like image and the high-frequency content from the panchromatic image, then integrated the resulting contents, which improved both the spectral and spatial information of the image.

Recent studies show curvelet transform gives a better result in image integration than multi-resolution and other methods. The Integration of SAR and visible-like images using curvelet transform gives better accuracy and higher reliability due to the characteristics of the technique, as mentioned above (Xiao et al., 2007). The method discussed in this study is the multi-scale curvelet transform combined method and extraction of spectral properties of images using horizontal cells of the retina to integrate SAR and visible-like images.

In this paper, some image integration techniques such as IHS transform, Brovey transform, feedback retina model, non-feedback retina model, wavelet transform, and curvelet transform are investigated to improve the spectral and spatial information of satellite images. In this research, three sets of images have been used, including Landsat-8, Sentinel-2 images, and Sentinel-1 images for the integration of SAR and visible-like images. Data collection, geometric and radiometric corrections, and coreference between input images have already been done. Also, a new algorithm has been proposed to improve the image quality resulting from the combination of SAR and visible-like images. In the proposed method, the curvelet transform is first applied to the three input levels of SAR and visible-like images, then using horizontal cells in the feedback retina model, spectral and spatial information below a specified and adjustable frequency is determined by a Gaussian low-pass filter and replaced with the curvelet coefficients of the integrated image approximation sub-band. Also, fine1 and detail1 sub-bands are selected from the visible-like image, and the coefficients of fine2, detail2 sub-bands are weighted and aggregated from both SAR and visible-like images in a specific way. Then, to evaluate the quality of the integrated images, two methods were presented: visual (human) comparison and computational comparison. Visual methods make comparisons based on the human visual system, so it has some problems in the evaluation process. Also, since people's visual perceptions are different, the computational comparison of image quality in recent decades has attracted further attention. The computational method is used to evaluate the spectral and spatial resolution of the resulting images.  $Q_I$ , ERGAS,  $Q^{AB/f}$ , MI, ED, and STD are among the different indexes for spectral and spatial quality evaluation of the integrated image. The present study aimed to integrate SAR and visible-like images of construction, vegetation, and coastal areas prepared by Sentinel 1, 2, and Landsat-8. To achieve a good spectral and spatial quality image using image integration techniques increases the accuracy of studies and can play an important role in helping the researchers. On the other hand, the more complete the information and spatial content, the greater the ambiguity in spectral information, so the purpose of integration is to provide an efficient way to achieve a reasonable state between these two opposite contradictory situations. In this regard, various integration methods were analyzed and quantitative and qualitative evaluation indicators were used to evaluate the efficiency of the methods regarding the improvement of spectral and spatial information.

## 2. Materials and Methods

### 2.1. The Study Area

Ahvaz is the capital city of Khuzestan province with an area of 222 km<sup>2</sup>, which is located at 48° 12' N 49° 12' E longitude of Greenwich meridian, and Oslo is the capital city of Norway with an area of 454.03 km<sup>2</sup>, which is located at 59° 54' N 10° 44' E longitude of Greenwich meridian. In this paper, part of Ahvaz, including residential areas and streets, were studied as construction areas, as well as parts of the harbor around Oslo city as vegetation and coastal areas.

### 2.2. Data

In the present study, Landsat-8 bands 2, 3, 4, and Sentinel-2 visible bands with a spatial resolution of 30m were used as multispectral images and for C-band integration; Sentinel-1 satellite with a spatial resolution of 10m was used as the SAR image. Matlab R14 software was also used to perform some necessary pre-processing, implementation of various integration methods, and to analyze the results of the simulations. In remote sensing, prior to the integration process, application of some necessary pre-processing such as radiometric correction, co-referencing and histogram matching of input images are essential because of the dissimilar imaging conditions and the different nature of the radar and visible-like images (Wang et al., 2016). The most important pre-processing in image integration is to ensure that the two images are co-referent. Therefore, both images must first be co-referenced separately using appropriate control points with the desired accuracy (Liu et al., 2016). In the present study, data collection, geometric and radiometric corrections, and reference between input images have already been done, and to decrease the execution time of the program, images were separated and used as decreased data using a small window.

On the other hand, one of the major problems with radar images is the presence of speckle noise. Speckle noise is caused by the coherent interference of reflected waves from many scatters such as earth, trees, and objects (Do and Vetterli, 2005). Speckle noise complicates the processing and interpretation of images, so it should be controlled. Applying noise removal techniques to images can fail to keep some of the information and reduce their resolution. Therefore, it is very important to filter out the noise to effectively use the images so that the information and resolution of the images are preserved. For this purpose, image processing techniques such as the use of a weighted median filter and histogram matching are applied to the input images to increase brightness and reduce artifact.

### 2.2 Integration Methods

#### 2.2.1. Brovey Transform

One of the most well-known pixel-level image integration algorithms is the Brovey method. According to this method, the visible-like image bands (multi-spectral images) are normalized and then multiplied by the Sentinel-1 satellite image single-band (SAR). Brovey method can be formulated by equation 1, (Choi, 2006). In fact, the algorithm, by normalizing the visible-like image bands, matches its brightness and contrasts with the SAR image.

$$Red = \frac{R}{R + G + B} * I_{SAR}$$

$$Red = \frac{G}{R + G + B} * I_{SAR} \tag{1}$$

$$Red = \frac{B}{R + G + B} * I_{SAR}$$

In the above equations, the parameters R, G, B represent the visible-like (multi-spectral) image bands and the  $I_{SAR}$  represents the SAR image band.

### 2.2.2. IHS Transform

IHS transform-based algorithms receive often great attention because of their ease of computation and high spatial resolution. This transform transfers the visible-like image bands from the RGB space to the IHS. After that, the mean and variance of the SAR image are matched with the intensity component obtained by applying the IHS transform to the visible-like image according to Equation 2, and then the inverse IHS transform is applied. The output of this process will be the same integrated image based on the IHS technique Brovey method can be formulated by equation 2, (Klonus and Ehlers, 2008):

$$I_{SAR_{adj}} = \frac{\sigma_I}{\sigma_{SAR}} [(I_{SAR} - \mu_{SAR}) + \mu_I] \quad (2)$$

In the above equation,  $\mu_{SAR}$ ,  $\mu_I$  and  $\sigma_{SAR} \cdot \sigma_I$  are the mean of the SAR single-band image, the intensity component of I, and their standard deviation, respectively. Also,  $I_{SAR_{adj}}$  is SAR adapted (adjusted) single-band image are used for replacement.

### 2.2.3. Discrete Wavelet Transform (DWT)

Wavelet transform is one of the most important image integration methods in pixel level based on the filtering in the frequency domain. By applying the wavelet transform to the input images, four sub-images, or four frequency sub-bands, are created, including Low-Low, Low-High, High-Low, and High-High. For the second level, the wavelet transform decomposition is performed on Low-Low. The wavelet decomposition can be continued until for N level of decomposition, the  $3N+1$  layer is obtained. The integration process takes place on the decomposed layers of the input images. The absolute value of wavelet transform coefficients provides important information on properties such as edges and lines. Therefore, calculating the maximum absolute value is an appropriate integration principle. In this regard, the absolute values of the layers are compared one by one and, if they are larger, placed in the corresponding layer of the final image. In this study, the integration process is performed at the second level of decomposition, because in most the prominent features of the image are better visualized. Therefore, the selection of the appropriate level of decomposition results in a better integration.

### 2.2.4. Integration of Sensors' Information Based on the Retina Model

The human visual system is one of the most efficient systems for image analysis. Each of the different parts of the eye plays an important role in the visual process. In many of the advanced imaging systems presented so far, various aspects of the human visual system have been attempted to be modeled so that the designed system has a function similar to that of the human visual system.

#### 2.2.4.1. Integration of Sensors' Information Based on the Non-Feedback Retina Model

The modeling of information received by cone and horizontal cells of retina and ultimately the created image in the brain can be described as follows: information obtained by cone cells and the horizontal cells are modeled with the Gaussian low-pass filter with  $\sigma_c$  cut-off frequency and Gaussian low-pass filter with  $\sigma_s$  cut-off frequency, respectively. On the other hand, as cone cells are sensitive to detail, they have a higher spatial resolution than horizontal cells, thus their filter bandwidth is much wider than the horizontal cells (Veloie and Ghassemian, 2005). In this model, the low-frequency and spectral content of the horizontal cells and the high frequency and spatial content of the cone cells from two completely separate paths pass through and from the image in the brain. Based on this model, for image integration, high-frequency information and low spatial frequency information (spectral content) should be extracted from high spatial resolution SAR image (similar to a cone cell) and visible-like multispectral image (similar to a horizontal cell), respectively. Accordingly, the integrated image is obtained by the equations 3, (Lotfi and Ghassemian, 2015):

$$F(u, v) = I_{SAR}(u, v) \cdot e^{-(u^2+v^2) \cdot 2\pi^2 \sigma_c^2} + I_{Optic}(u, v) \cdot e^{-(u^2+v^2) \cdot 2\pi^2 \sigma_s^2} \quad (3)$$

In the above equation, the parameters  $\sigma_s, \sigma_c$  are the width of the Gaussian centre receptive field (cone cells) and the Gaussian surround receptive field (horizontal cells), respectively ( $\sigma_s > \sigma_c$ ). Therefore, the Gaussian surround receptive field is narrower in the frequency domain.

#### 2.2.4.2. Integration of Sensors' Information Based on the Feedback Retina Model

In the no-feedback retina model, the inhibitory effect of horizontal cells on cone cells should also be taken into account to better and fully describe the centre-surround structure created by the contrast. The effect is accounted for by the feedback path from horizontal cells to cone cells. Based on this model, the spatial information lower than a specified frequency and the spatial information higher than this frequency are obtained by a Gaussian low-pass filter from the multispectral image and the Difference of Gaussian (DOG) from SAR image (Daneshvar and Ghassemian, 2011). In fact, the role of horizontal cells in this model is to extract spectral features from the multispectral image (Veloie and Ghassemian, 2005). In other words, the Gaussian low-pass filter well preserves the spectral and low frequency detail of the multi-spectral image; however their spatial detail is reduced. Adding detail extracted from SAR images by DOG will result in acceptable spectral and spatial quality. Considering the effect of horizontal cells on cone cells, frequency response of bipolar cell is obtained by equation 4, (Veloie and Ghassemian, 2005):

$$H(u, v) = (e^{-(u^2+v^2) \cdot 2\pi^2 \sigma_c^2} - k_{hc} \cdot e^{-(u^2+v^2) \cdot 2\pi^2 \sigma_s^2}) + e^{-(u^2+v^2) \cdot 2\pi^2 \sigma_s^2} \quad (4)$$

In the above equation, the parameters  $\sigma_s, \sigma_c$  are the width of the Gaussian centre receptive field (cone cells) and the Gaussian surround receptive field (horizontal cells), respectively. The parameter ( $k_{hc} = \frac{1}{\Delta^2}$ ) is also the feedback gain to apply the horizontal cells inhibitory effect on the cone cells. The parameter  $\Delta$  indicates the ration of spatial resolution of the visible multispectral image (30 m) to the spatial resolution of the SAR image (10 m), equal to 3 for the images used in this study. The frequency response of the mentioned filters and the integrated image based on the general formula proven for the bipolar cell is obtained by the equations (5), (6), (7) as follows [23] and assuming  $\sigma_s = \Delta \sigma_c = 3\sigma_c$ :

$$H_{SAR}(u, v) = H_{\frac{-1}{1, \frac{1}{\Delta^2}, \sigma_c, 3\sigma_c}}(u, v) = (e^{-(u^2+v^2) \cdot 2\pi^2 \sigma_c^2} + \frac{-1}{\Delta^2} \cdot e^{-(u^2+v^2) \cdot 2\pi^2 (3\sigma_c)^2}) \quad (5)$$

$$H_{Optical}(u, v) = H_{0, 1, \sigma_c, 3\sigma_c}(u, v) = (e^{-(u^2+v^2) \cdot 2\pi^2 (3\sigma_c)^2}) \quad (6)$$

$$F(u, v) = I_{SAR}(u, v) \cdot H_{SAR}(u, v) + I_{Optical}(u, v) \cdot H_{Optical}(u, v) \quad (7)$$

According to the above equations, the only adjustable parameter in this model is  $\sigma_c$  (0.02 to 0.05, minimum *height and width* of the *image*). In this study, 0.05 was also considered as the most appropriate value for  $\sigma_c$ . In the final step, the new intensity image obtained by feedback retina model replacing with the intensity component obtained by IHS transform is transferred to the visible-like image and into the RGB space.

### 3. Proposed Method

Curvelet transform is one of the new emerging methods of multi-resolution analysis, which does not have many shortcomings of other multi-scale analysis methods. This transform is capable of directly detecting edges and curved shapes in images. Curvelet transform is actually a nonstandard multidimensional-multi-scale pyramid with many geometrical orientations at each scale, so it does not have wavelet transform deficiencies in detecting edges, with a much robust and less sensitive structure against the noise. By applying the curvelet transform to an image, at the first level of decomposition, the coefficients of the approximation sub-band are created, with a content similar to the low-low sub-band in the wavelet transform; and after the second level of decomposition, three coefficients, including approximation, non-standard fine and detail orientation sub-bands are prepared. In this study, a new algorithm was used for integration of the curvelet transform coefficients based on the application of horizontal cells in the retina model which is presented in

Figure 1.

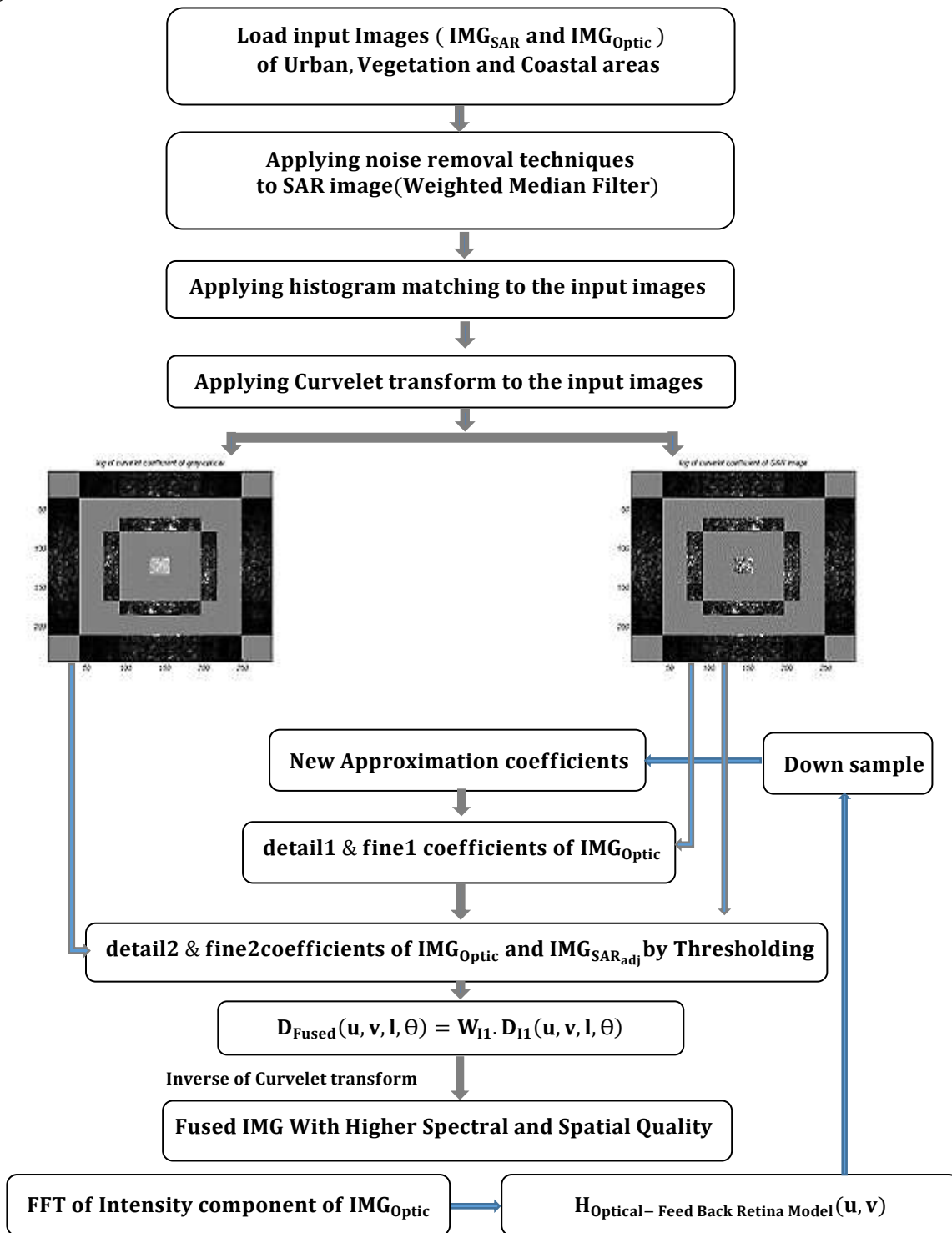


Figure 1. Diagram of proposed method.

To implement the proposed method, after making the necessary pre-processing, the curvelet transforms to three levels of decomposition is first applied to the input images. Then, considering the use of horizontal cells to extract the spectral properties of images in the feedback retina model, the spectral and spatial information lower than the specified and adjustable frequency is found from the visible-like image by a

Gaussian low-pass filter with  $\sigma_s$  cut-off frequency. After that, sampling is performed from the output of the Gaussian with a decreasing coefficient and the obtained coefficients are replaced with the coefficients of the integrated image approximation sub-band. The coefficients of the fine1, detail1 sub-bands are then selected from the visible-like image because they are smaller than the coefficients of the SAR image. Next, we weight the coefficients of detail 2 and fine 2 sub-band from both SAR and visible-like images according to the following steps:

Calculate the information and content of the curvelet coefficients by considering their neighbourhood at different scales of curvelet transform and the degree of conformity of the corresponding windows of input images in the corresponding sub-bands. In this regard, given the values of the neighbouring coefficients, we consider a window of  $5 * 5$  to calculate the content of its curvelet coefficient of central location, and calculate the energy parameter  $E_{I_1}(u, v, l, \theta)$ ,  $E_{I_2}(u, v, l, \theta)$  according to equation (8) and (9). In addition, the conformity of corresponding windows in the corresponding sub-bands is determined according to equation 10, (Burt and Kolczynski, 1993):

$$E_{I_1}(u, v, l, \theta) = \sum_{s,t=1}^5 \rho(X) |D_{I_1}(u + s, v + t, l, \theta)|^2 \quad (8)$$

$$E_{I_2}(u, v, l, \theta) = \sum_{s',t'=1}^5 \rho(Y) |D_{I_2}(u + s', v + t', l, \theta)|^2 \quad (9)$$

$$M_{I_1, I_2}(u, v, l, \theta) = \frac{2 \sum_{s,t=1}^5 \rho(X, Y) D_{I_1}(u + s, v + t, l, \theta) D_{I_2}(u + s, v + t, l, \theta)}{E_{I_1}(u, v, l, \theta) + E_{I_2}(u, v, l, \theta)} \quad (10)$$

In the above equation, the parameters  $M_{I_1, I_2}$ ,  $s', t', s, t$ ,  $D_I(u, v, l, \theta)$ , and  $(u, v, l, \theta)$  represent the degree of conformity of the windows  $\rho(X)$ ,  $\rho(Y)$ , their dimension, the curvelet coefficients, and their position in the coordinates  $(u, v)$  at level  $l$  and direction  $\theta$ . Calculate the optimal threshold for the conformity of the corresponding windows to weight the central curvelet coefficients in the corresponding windows. Now, equations (13) and (14) are defined so that the weights  $W_{min}$  and  $W_{max}$  are normalized 0 to 1. Hence, we thus assume  $T = 0.5$  as the appropriate threshold for this interval. The maximum and minimum weights are also calculated according to equations (11), (12), (13), (14) (Burt and Kolczynski, 1993):

$$W_{min} = \frac{1}{2} - \frac{1}{2} \left( \frac{1 - M_{I_1, I_2}(u, v, l, \theta)}{1 - T} \right) \quad (11)$$

$$W_{max} = 1 - W_{min} \quad (12)$$

if the conformity of corresponding windows is higher than the threshold, then:

$$M_{I_1, I_2}(u, v, l, \theta) > T \rightarrow \begin{cases} E_{I_1}(u, v, l, \theta) > E_{I_2}(u, v, l, \theta), \\ \{W_{I_1} = W_{max}\} \\ \{W_{I_2} = W_{min}\} \end{cases} \quad (13)$$

else if  $E_{I_2}(u, v, l, \theta) > E_{I_1}(u, v, l, \theta)$ ,  $\begin{cases} W_{I_2} = W_{max} \\ W_{I_1} = W_{min} \end{cases}$

and if the conformity of corresponding windows is lower than the threshold, then:

$$\begin{aligned}
 M_{I_1, I_2}(u, v, l, \theta) < T \rightarrow E_{I_1}(u, v, l, \theta) > E_{I_2}(u, v, l, \theta), \begin{cases} W_{I_1} = 1 \\ W_{I_2} = 0 \end{cases} \\
 \text{else if } E_{I_2}(u, v, l, \theta) > E_{I_1}(u, v, l, \theta), \begin{cases} W_{I_2} = 1 \\ W_{I_1} = 0 \end{cases}
 \end{aligned} \tag{14}$$

In the above equations, the parameters  $W_{I_1}$ ,  $W_{I_2}$ ,  $E_{I_1}$ ,  $E_{I_2}$ , and  $M_{I_1, I_2}$  are the weights obtained for the coefficients of detail 2 and fine 2, curvelet transform coefficients energy, and the conformity of the curvelet coefficients content in the corresponding windows of visible-like and SAR images in the corresponding sub-bands, respectively. Finally, we apply the inverse curvelet transform to the  $D_{Fused}(u, v, l, \theta)$  integrated curvelet coefficients and calculate the final integrated image according to equation 15, (Shokrallahi and Sahebi, 2017):

$$D_{Fused}(u, v, l, \theta) = W_{I_1} \cdot D_{I_1}(u, v, l, \theta) + W_{I_2} \cdot D_{I_2}(u, v, l, \theta) \tag{15}$$

The proposed method has been performed by applying two and five levels of curvelet decomposition to SAR and visible-like images. All the steps were exactly same as the proposed method in three levels of curvelet decomposition, except that the weighting of the curvelet coefficients of visible-like and SAR images was performed by applying the two levels of curvelet decomposition to the coefficients of fine1, detail1, and five levels of curvelet decomposition to the coefficients of fine 3, detail 3, fine 4, and detail 4 sub-bands.

## 4. Results

### 4.1. Implementation Evaluation results of the Algorithms according to Visual and Qualitative Criteria

By visual interpretation of the integrated images and comparing them with the input images, one can detect changes in color quality, sharpness of edges, lines and effects. However, this criterion alone is not appropriate for accurate examination and analysis of the spectral and spatial quality of the images.

### 4.2. Simulation Evaluation results of Different Integration Algorithms on Construction, Urban, Vegetation, and Coastal Areas

The visual results of the integrated images obtained from the implementation of Brovey and IHS algorithms, wavelet transform, no-feedback retina model, feedback retina model, curvelet transform are presented in Figures 1 to 3. We have used three sets of images, including Landsat-8, Sentinel-2 images and Sentinel-1 images for the integration of SAR and visible-like images. In this paper, part of Ahvaz, including residential areas and streets, were studied as construction areas, Figures (2a) to (2j), as well as parts of the herbor around Oslo city as vegetation Figures (3a) to (3j), and coastal areas Figures (4a) to (4j). Visual comparison of the results shows the high spectral quality and the sharpness of the proposed method, especially at the second level of decomposition compared to other methods.

#### 4.2.1. Simulation results of Different Integration Algorithms on Construction, Urban Areas

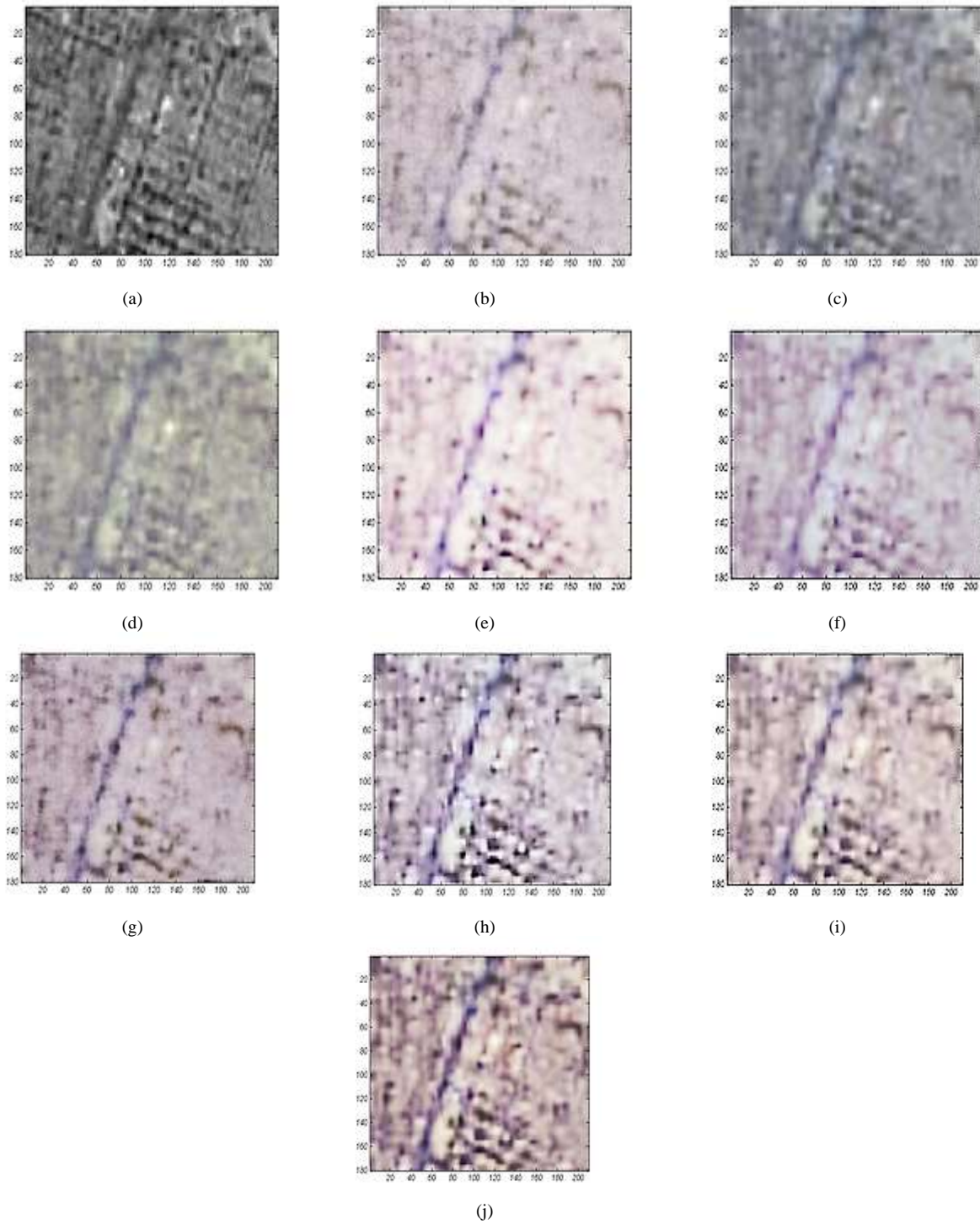


**Figure 2.** Dataset (1): (a) SAR image; (b) Optic image. Fused images: (c) Brovey; (d) IHS; (e) Non-Feedback retina model; (f) Feedback retina model; (g) WT; (h) Curvelet; (i) Proposed method in third decomposition; (j) Proposed method in the second decomposition.

## 4.2.2. Simulation results of Different Integration Algorithms on Vegetation Areas

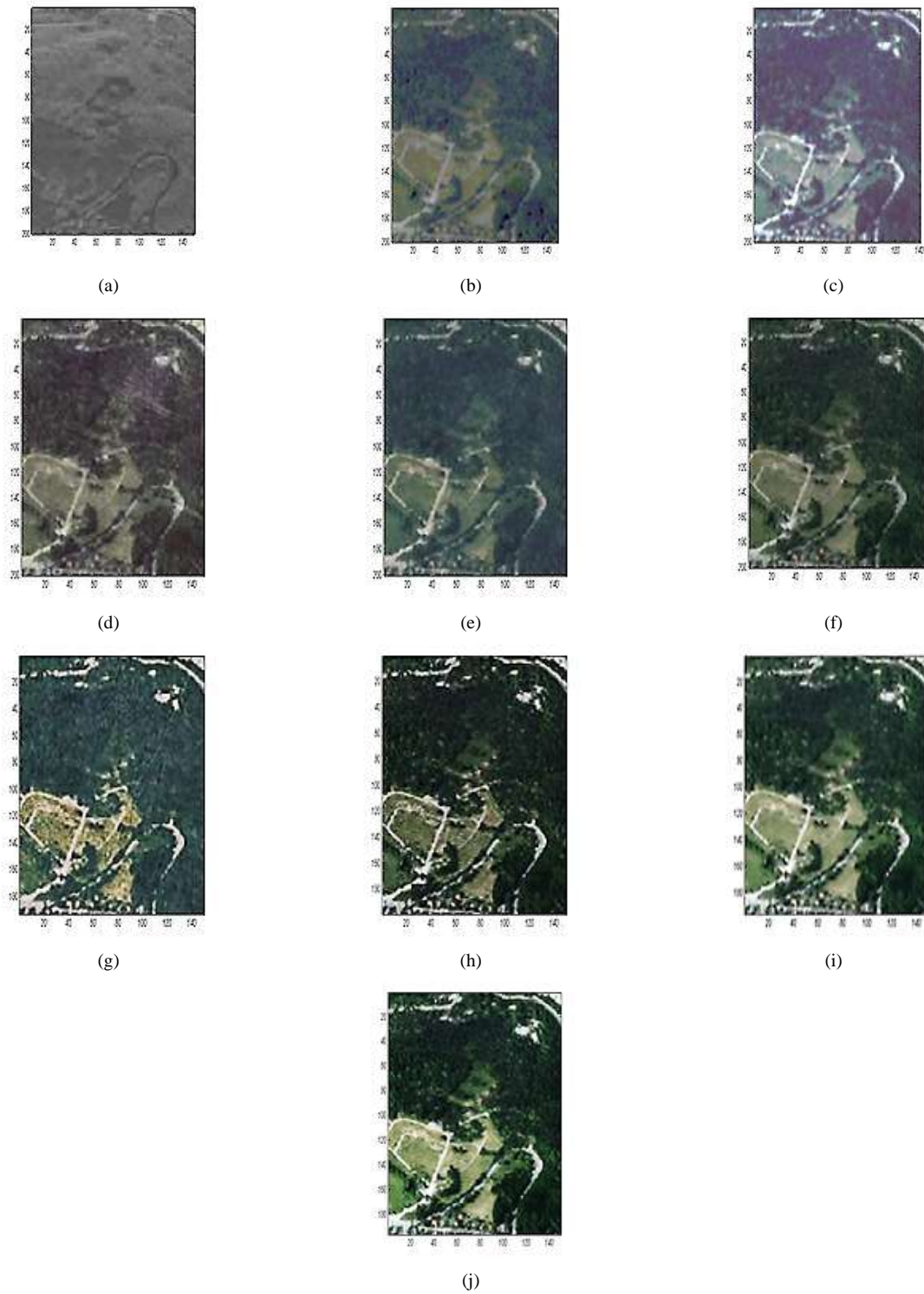


**Figure 3.** Dataset (2): (a) SAR image; (b) Optic image. Fused images: (c) Brovey; (d) IHS; (e) Non-Feedback retina model; (f) Feedback retina model; (g) WT; (h) Curvelet; (i) Proposed method in third decomposition; (j) Proposed method in the second decomposition.

### 4.2.3. Simulation results of Different Integration Algorithms on Coastal Areas

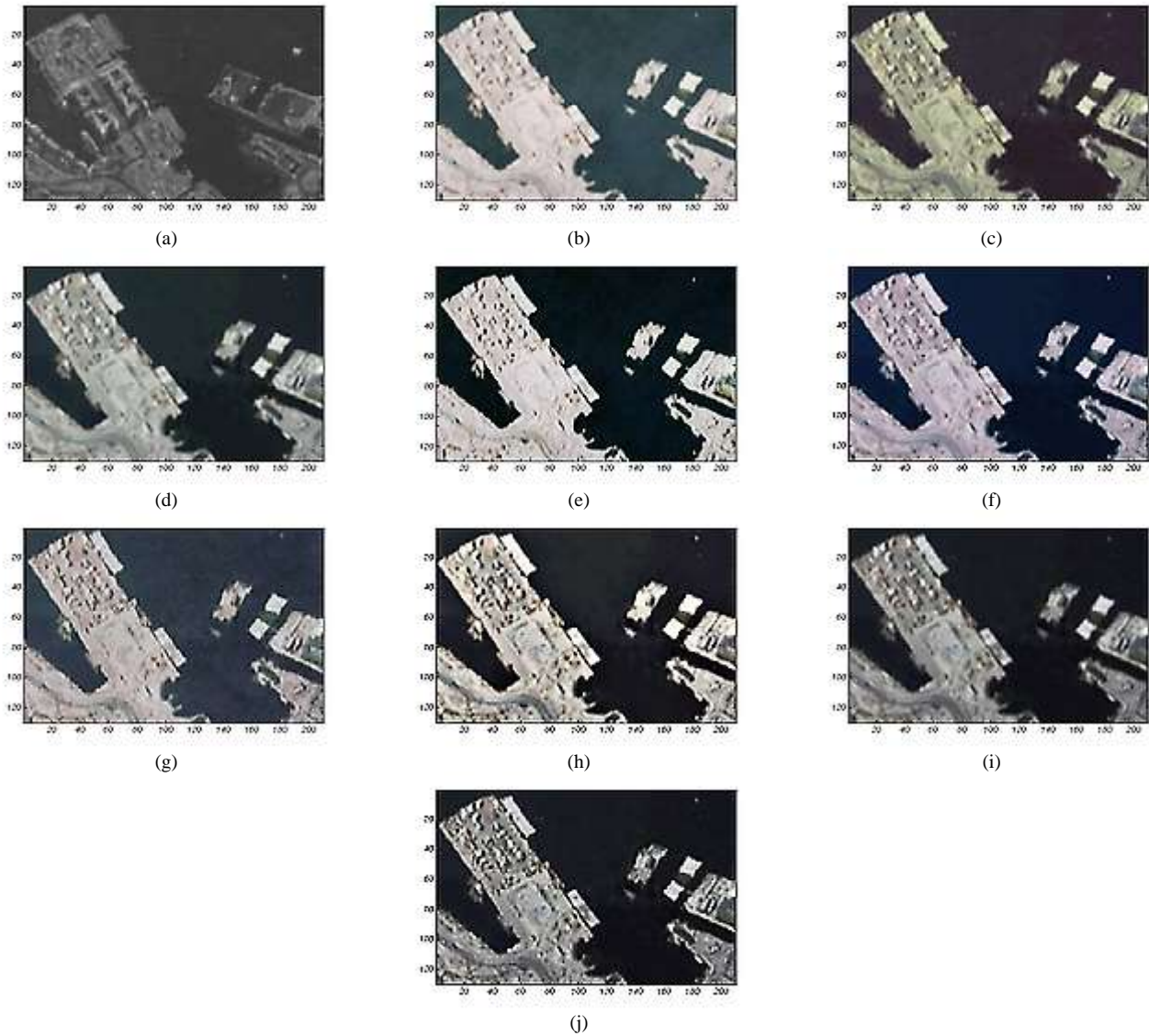


**Figure 4.** Dataset (3): (a) SAR image; (b) Optic image. Fused images: (c) Brovey; (d) IHS; (e) Non-Feedback retina model; (f) Feedback retina model; (g) WT; (h) Curvelet; (i) Proposed method in third decomposition; (j) Proposed method in the second decomposition.

### 4.3. Evaluation results of the Implementation of the Algorithms according to Quantitative Criteria

In this study, quality index, mutual information, relative dimensionless global error in system, integration information score, Euclidean distance, and standard deviation were used to evaluate the accuracy, spectral and spatial content of the integrated images.

#### 4.3.1. Integrated Information Score ( $Q^{(AB/\hat{f})}$ )

$Q^{(AB/\hat{f})}$  measure the amount of edge information transferred from the intensity component of the input image to the intensity component of integrated image. It is obtained according to equation 16, (Ma, and Li, 2019):

$$Q^{AB/f} = \frac{\sum_{i=1}^N \sum_{j=1}^M Q_g^{A,f}(i,j) \cdot Q_a^{A,f}(i,j) + Q_g^{B,f}(i,j) \cdot Q_a^{B,f}(i,j)}{\sum_{i=1}^N \sum_{j=1}^M Q_g^{A,f}(i,j) + Q_g^{B,f}(i,j)} \quad (16)$$

In the above equation, and  $Q_a^{B,f}(i,j)$  and  $Q_g^{B,f}(i,j)$  show the strength and direction of the edge at the position (i, j).

#### 4.3.2. Quality Index (QI)

One of the global indexes of quality assessment is the criterion of structural similarity. The index is calculated according to the equation 17, (Mahyari, and Yazdi, 2009), the better the performance of the integration method.

$$Q_{I_{X,F}} = \sum_{x,f} \frac{2\mu_x\mu_f}{\mu_x^2 + \mu_f^2} \cdot \frac{2\sigma_x\sigma_f}{\sigma_x^2 + \sigma_f^2} \cdot \frac{\sigma_{xf}}{\sigma_x\sigma_f} \quad (17)$$

In the above equation  $Q_{I_{X,F}}$ ,  $\sigma_x$ ,  $\sigma_{x,f}$ ,  $\sigma_f$ ,  $\mu_x$ , and  $\mu_f$  represent the structural similarity between the input and integrated images, the covariance and standard deviation of the input and integrated images, respectively, and the mean grey level of the input and integrated images, respectively. The total QI, between the input and integrated images, is obtained (Mahyari, and Yazdi, 2009), from equation 18:

$$Q_I = Q_{I_{A,F}} + Q_{I_{B,F}} \quad (18)$$

#### 4.3.3. Mutual Information (MI)

The MI is another indicator of quality assessment, which measures the amount of information transmitted from the input images to the integrated image. MI is a fundamental concept in information theory that measures the degree of dependence of two random variables and is defined by equation 19, (Ma and Li, 2019):

$$MI_{x,f} = \sum_{x,f} \rho_{x,f}(x,f) \cdot \log \frac{\rho_{x,f}(x,f)}{\rho_x(x) \cdot \rho_f(f)} \quad (19)$$

In the above equation,  $MI_{x,f}$ ,  $\rho_{x,f}(x,f) \cdot \rho_f(f)$ , and  $\rho_x(x)$  represent the amount of information transmitted from the input image to the integrated image, the marginal histogram probability density functions, and the common histogram probability density function of are the grey level of the input and integrated images, respectively. The total MI, between the input and integrated images, is obtained from the equation 20, (Sun and Deng, 2012)

$$MI = MI_{A,F} + MI_{B,F} \quad (20)$$

#### 4.3.4. Relative Dimensionless Global Error in System (ERGAS)

It is an extended index of the RMSE criterion and shows the spectral and spatial efficiency of the integration algorithm. It is obtained according to the equations (21 to 23), (Nencini et al., 2007; Reinoso and Moncayo, 2011):

$$Spectral \left\{ \begin{aligned} ERGAS_{spectral} &= 100 \frac{h}{l} \sqrt{\frac{\sum_{i=1}^{N_{Bands}} \frac{(RMSE_{spectral}(Band_i))^2}{(Multi_i)^2}}{N_{Bands}}} \\ RMSE_{spectral(Band_i)} &= \frac{1}{NP} \sqrt{\sum_{k=1}^{NP} (Multi_i(k) - FUS_i(k))^2} \end{aligned} \right. \quad (21)$$

$$Spatial \left\{ \begin{array}{l} ERGAS_{spatial} = 100 \frac{h}{l} \sqrt{\frac{\sum_{i=1}^{N_{Bands}} \frac{(RMSE_{spatial}(Band_i))^2}{(\overline{SAR}_i)^2}}{N_{Bands}}} \\ RMSE_{spatial(Band_i)} = \frac{1}{NP} \sqrt{\sum_{k=1}^{NP} (SAR(k) - FUS_i(k))^2} \end{array} \right. \quad (22)$$

$$ERGAS = \frac{ERGAS_{spectral} + ERGAS_{spatial}}{2} \quad (23)$$

In the above equations, the parameters  $l$ ,  $h$ ,  $N_{Bands}$ ,  $NP$ ,  $\overline{Multi}_i$  and  $\overline{SAR}_i$  are the spatial resolution of SAR image, intensity component of a visible-like image, number of bands in a visible-like image, number of pixels in input and integrated image, mean of SAR images, and intensity component of a visible-like image, respectively.

#### 4.3.5. Euclidean Distance (ED)

This type of spectral distance is defined on the basis of the spectral angle. Its fundamental difference with the spectral angle criterion is that the ED method is affected by the difference in luminosity between the spectra. The smaller this criterion is, the better the spectral quality of the integrated Image. This parameter is obtained according to equations (24 and 25), (Bigdeli et al., 2014):

$$SAM(A_i, F_i) = \cos^{-1} \left( \frac{\sum_{i=1}^N A_i \cdot F_i}{\sqrt{\sum_{i=1}^N A_i^2 \cdot \sum_{i=1}^N F_i^2}} \right) \quad (24)$$

$$ED(A_i, F_i) = 2 \cdot \sqrt{1 - \frac{\sum_{i=1}^N A_i \cdot F_i}{\sqrt{\sum_{i=1}^N A_i^2 \cdot \sum_{i=1}^N F_i^2}}} = 2 \cdot \sin \left( \frac{SAM(A_i, F_i)}{2} \right) \quad (25)$$

In the above equation,  $N$ ,  $A = (A_1, A_2, \dots, A_N)$ ,  $F = (F_1, F_2, \dots, F_N)$ , and  $SAM$  are the number of bands, the spectral vectors of the visible-like and integrated images, and the angle of deviation in a pixel of the image. The closer the ED is to zero, the higher the spectral information is.

#### 4.3.6 Standard Deviation (STD)

This parameter indicates the contrast of the image and shows the distribution of grey level of the image relative to the mean. The larger standard deviation indicates more information. The standard deviation is obtained according to equation 26, (Li et al., 2008):

$$STD = \frac{1}{MN} \sqrt{\sum_{i=1}^N \sum_{j=1}^M |g_{i,j} - \bar{g}|^2} \quad (26)$$

In the above equation,  $g_{i,j}$  and  $\bar{g}$  the grey level of a pixel and the mean of grey level, respectively.

#### 4.3.7 Numerical results of Quantitative Parameters Derived from Algorithm Implementation

Numerical values of spectral and spatial parameters to investigate and interpret the results are presented in Table 1.

**Table 1.** Calculated Numerical Values of Spectral and Spatial Parameters.

<b>Construction and Urban Areas</b>	<b>Q<sup>(AB/f)</sup></b>	<b>Q<sub>I</sub></b>	<b>MI</b>	<b>ERGAS</b>	<b>ED</b>	<b>STD</b>
Brovey	0.5792	0.3906	2.0925	0.0561	1.6735	37.4920
IHS	0.5068	0.4236	1.9027	0.0583	1.8972	36.1287
DWT	0.3927	0.2637	1.7063	0.0488	1.1219	38.4731
Non-Feedback Retina Model	0.2904	0.3162	1.8649	0.0674	1.2157	35.2719
Feedback Retina Model	0.6143	0.5473	3.2160	0.0427	1.0584	40.4880
Curvelet	<b>0.7559</b>	0.6058	3.8723	0.0418	0.5308	46.1358
Proposed method method in 2th decomposition	0.7105	<b>0.8619</b>	<b>4.3429</b>	<b>0.0346</b>	<b>0.3461</b>	<b>57.3765</b>
Proposed method method in 3th decomposition	0.6742	0.8365	4.2087	0.0392	0.3958	53.1402
<b>Vegetation Areas</b>	<b>Q<sup>(AB/f)</sup></b>	<b>Q<sub>I</sub></b>	<b>MI</b>	<b>ERGAS</b>	<b>ED</b>	<b>STD</b>
Brovey	0.5042	0.6582	2.7509	0.0642	1.4760	40.0952
IHS	0.4871	0.6127	2.0943	0.0591	1.6824	39.5603
DWT	0.4619	0.6289	2.9365	0.0583	1.0147	41.8194
Non-Feedback Retina Model	0.3804	0.5061	1.7210	0.0627	1.1949	37.8925
Feedback Retina Model	0.6741	0.7639	3.0623	0.0589	0.9531	43.8327
Curvelet	0.7563	0.7640	3.9751	0.0523	0.4779	48.3091
Proposed method method in 2th decomposition	<b>0.8139</b>	<b>0.9146</b>	<b>4.1217</b>	<b>0.0507</b>	<b>0.2903</b>	<b>54.7245</b>
Proposed method method in 3th decomposition	0.7951	0.8975	3.2937	0.0539	0.3421	52.3360
<b>Coastal Areas</b>	<b>Q<sup>(AB/f)</sup></b>	<b>Q<sub>I</sub></b>	<b>MI</b>	<b>ERGAS</b>	<b>ED</b>	<b>STD</b>
Brovey	0.5936	0.6901	2.8150	0.0614	1.5304	37.1296
IHS	0.5231	0.5726	2.1704	0.0637	1.7285	36.9905
DWT	0.4819	0.6210	2.9863	0.0596	1.1920	38.7852
Non-Feedback Retina Model	0.4486	0.5014	1.9427	0.0651	1.4290	35.6125
Feedback Retina Model	0.6907	0.6295	3.5168	0.0574	1.1701	41.9810
Curvelet	<b>0.8671</b>	0.6781	4.1804	<b>0.0436</b>	0.5037	45.7854
Proposed method method in 2th decomposition	0.8397	<b>0.8604</b>	<b>4.3172</b>	0.0513	<b>0.3617</b>	<b>49.0371</b>
Proposed method method in 3th decomposition	0.8152	0.8523	3.8249	0.0527	0.3916	47.6027

As is evident, the proposed method has a significant advantage over other methods due to its quantitative value of spectral and spatial parameters.

## 5. Discussion and Conclusion

By intuitive examination of the integrated images, it is found that all the implemented algorithms except the Brovey and IHS have relatively better spectral properties and content compared to the visible-like image. In fact, the most important drawback in IHS is the degradation of spectral and color content. Also in the Brovey method, due to the modulation of the spatial information of the SAR image on the content of each band of the visible-like image, there is a significant spectral and color distortion in the integrated images, especially for the construction areas. In contrast, the proposed method, the curvelet transform, and feedback retina models have the best performance in preserving and transferring the properties and spectral contents, respectively. In the proposed method, in the feedback retina model, horizontal cells were used to extract the spectral features of the visible-like image. On the other hand, due to the adjustability of the parameter  $\sigma_c$  and the width of the Gaussian low-pass filter receptive field, a better approximation sub-band was replaced with the curvelet coefficients of the integrated image approximation sub-band, so the spectral properties of the integrated image vividly improved compared to other methods.

The ED parameter values (0.0364, 0.2903, 0.3617), in Table 1, which is a quantitative criterion for comparing the spectral difference between the integrated image and the input image, confirm the high performance of the proposed integration methods in preserving spectral properties and content. The color change is observed in all integration algorithms and is unavoidable, but a careful comparison of the results can show that the integration of SAR and visible-like images based on Brovey and IHS transform has a significant color distortion. While the color distortion created in other methods is relatively acceptable.

Considering the  $Q^{(AB/f)}$  parameter values (0.7559, 0.8139, 0.8671), in Table 1, which is a quantitative criterion for comparing the power of algorithms in detecting edges of the image, it is found that the curvelet

method and the proposed method have the highest performance at the second level of decomposition, and the Brovey transform, IHS transform and the feedback retina model have relatively acceptable performance in preserving and detecting edges. The superiority of the proposed method and crawl transform is due to the nature of crawl transform in the direct detection of a variety of edges and image details. In contrast, the wavelet transform method and no-feedback retina model have the weakest performance in preserving and detecting edges. In the wavelet transform method, with increasing levels of decomposition, more spatial information and content is transferred to the output, but the spectral content is degraded. The wavelet transforms at the second level of decomposition has an acceptable performance in preserving the spectral properties, though ineffective in detecting edges.

Considering the ERGAS parameter values (0.3461, 0.0507, 0.0436), in Table 1, it is found that the curvelet method and the proposed method have the minimum spectral and spatial error, which show that the proposed algorithm is accurate and reliable.

According to the values of  $Q_i$ , MI, STD parameter, in Table 1, it is suggested that the proposed method has the ability to maximize information from the incoming images to the integrated image. The reality of all studies in the field of image integration is that the claim of absolute separation of spatial and spectral properties is impossible. In other words, increasing spatial accuracy will degrade spectral information, and as the spatial information and content become more complete, the ambiguity in spectral information increases (Veloie and Ghassemian, 2005). The aim of integration is therefore to provide an efficient way to arrive at a reasonable amount between these two contradictory situations. Based on the visual interpretation of the integrated images and the results of Table 1, the proposed method in the second level of decomposition after the curvelet transform has the best spatial resolution in the construction and coastal areas. However, considering the quality index, mutual information, relative dimensionless global error in the system, and standard deviation, the method has the highest spectral and spatial quality, significantly enhancing the spectral properties and providing high spatial resolution.

## Acknowledgements

The authors hereby express their gratitude to the Iranian Space Research Center, Shiraz Institute of Mechanics, for providing data and financial support for the present project, under the title of research project No. (6) of the contract of 96/1050/420 with shiraz university.

## References

- Agrawal, D., & Karar, V. (2018). Generation of enhanced information image using curvelet-transform-based image fusion for improving situation awareness of observer during surveillance. *International journal of Image and Data Fusion*, 10(1), 45-57.
- Bigdeli, B., Weldanzouj, M. J., & Maghsoudi Mehrani, Y. (2014). Assessing OLI's Measuring Potential in Separating Six Iranian Wheat Varieties Using a Spectral Library. *Scientific-Research Quarterly, Geographical Information*, 24(93).
- Burt, P., & Adelson, E. (1983). The Laplacian pyramid as a compact image code. *IEEE Transactions on communications*, 31(4), 532-540.
- Burt, P. J., & Kolczynski, R. J. (1993, May). Enhanced image capture through fusion. In *1993 (4th) international Conference on Computer Vision* (pp. 173-182). IEEE. Doi:<https://dx.doi.org/10.1109/ICCV.1993.378222>.
- Candes, E., Demanet, L., Donoho, D., & Ying, L. (1999). Fast discrete curvelet transforms. *Multiscale modeling & Simulation*, 5(3), 861-899.
- Choi, M. (2006). A new intensity-hue-saturation fusion approach to image fusion with a trade-off parameter. *IEEE Transactions on Geoscience and remote sensing*, 44(6), 1672-1682.
- Daneshvar, S., & Ghassemian, H. (2011). MRI and PET image fusion by combining IHS and retina- inspired models. *Information fusion*, 11(2), 114-123.
- Dong, L., Yang, Q., Wu, H., Xiao, H., & Xu, M. (2015). High quality multi-spectral and panchromatic image fusion technologies based on Curvelet transform. *Neurocomputing*, 159, 268-274.

- Do, M. N., & Vetterli, M. (2005). The contourlet transform: an efficient directional multiresolution image representation. *IEEE Transactions on image processing*, 14(12), 2091-2106.
- Klonus, S., & Ehlers, M. (2008, November). Pan sharpening with TerraSAR-X and optical data. In *3<sup>rd</sup> terraSAR-X Science Team Meeting* (pp. 25-26).
- Lau, W., King, B. A., & Li, Z. (2000). The influences of image classification by fusion of spatially oriented images. *International Archives of Photogrammetry and Remote Sensing*, 33(B7/2; PART 7), 752-759.
- Li, S., & Yang, B. (2008). Multifocus image fusion by combining curvelet and wavelet recognition letters, 29(9), 1295-1301.
- Liu, J., Gong, M., Qin, K., & Zhang, P. (2016). A deep convolutional coupling network for change detection based on heterogeneous optical and radar images. *IEEE transactions on neural networks and learning systems*, 29(3), 545-559.
- Li, Y., Xu, X., Bai, B. D., & Zhang, Y. N. (2008, July). Remote sensing image fusion based on fast discrete curvelet transform. In *2008 international conference on machine learning and cybernetics* (Vol. 1, 106-109).
- Lotfi, M., & Ghassemian, H. (2015). Combined Retina model and improved adaptability IHS to fusion remote sensing images. 23<sup>rd</sup> Iranian Conference on Electrical Engineering, Tarbiat Modarres university School of Electrical and Computer Engineering.
- Ma, J., Ma, Y., & Li, C. (2019). Infrared and visible image fusion methods and applications: A survey. *Information Fusion*, 45, 153-178.
- Mahyari, A. G., & Yazdi, M. (2009, March). A novel image fusion method using curvelet transform based on linear dependency test. In *2009 International Conference on Digital Image Processing* (pp. 351- 354). IEEE.
- Mitchell, H. B. (2007). *Multi-sensor data fusion: an introduction*. Springer Science & Business Media.
- Nencini, F., Garzelli, A., Baronti, S., & Alparone, L. (2007). Remote sensing image fusion using the based curvelet transform. *Information fusion*, 8(2), 143-156.
- Pappas, O. A., Achim, A. M., & Bull, D. R. (2013, August). Curvelet fusion of panchromatic and SAR satellite imagery using fractional lower order moments. In *2013 10th IEEE International Conference on advanced Video and Signal Based Surveillance* (pp. 342-346). IEEE.
- Reinoso, J. F., & Moncayo, M. (2011). Optimal quality for image fusion with interpolatory parametric filters. *Mathematics and Computers in Simulation*, 81(10), 2307-2316.
- Retrieved from: <https://faradars.org/courses/fvdm9405-data-fusion-strategy>
- Shahab pour, M., & Yazdi, M. (2013). Segmentation of SAR images using neural network training by bee colony algorithm. First National Conference on innovation in computer engineering and information, Shafaq Institute of higher Education.
- Shokrallahi, M., & Sahebi, M. (2017). Fusion of Polari metric and hyper spectral data to classify land cover. Master thesis. Khaje Nasirtoosi University of Technology, School of surveying Engineering.
- Sun, P., & Deng, L. (2012, June). An image fusion method based on region segmentation and wavelet transform. In *2012 20th International Conference on Geoinformatics* (pp. 1-5). IEEE.
- Veloie, M., & Ghassemian, H. (2005). Integrate sensor image information into remote sensing application (Inspired by the retina model). Ph.D. Thesis, Tarbiat Modarres university School of Electrical and computer Engineering.
- Wang, Q., Shi, W., Atkinson, P. M., & Wei, Q. (2016). Approximate area-to-point regression kriging for fast hyperspectral image sharpening. *IEEE Journal of Selected Topics in Applied Earth Observations and Remote Sensing*, 10(1), 286-295.
- Xiao, M., He, Z., & Jia, Y. (2007, August). Fusion of multisensor images based on the curvelet transform. in *Geoinformatics 2007: Remotely Sensed Data and Information* (Vol. 6752, p. 675200). International society for Optics and Photonics.